The Surface Roughness of Large Craters on Mercury

Hannah C. M. Susorney,[1,2] Olivier S. Barnouin,[3,4] Carolyn M. Ernst,[3] and Angela M. Stickle[3]

Corresponding author: H. C. M. Susorney, Department of Earth, Atmospheric and Ocean Sciences, University of British Columbia, Vancouver, B.C., V6T 1Z4, Canada (hsusorney@eoas.ubc.ca)

[1]Department of Earth and Planetary

Key Points.

- For horizontal scales less than 10km, ejecta related processes drive surface roughness around large craters
- Surface roughness at scales of 0.5–250 km are not correlated with crater density (diameters of 20-120 km).

Abstract. This study investigates how individual large craters on Mercury (diameters of 25–200 km) can produce surface roughness over a range of baselines (the spatial horizontal scale) from 0.5 ? 250 km. Surface roughness is a statistical measure of change in surface height over a baseline after topography has been detrended. We use root-mean-square (RMS) devi-

Science, The Johns Hopkins University, Baltimore, MD 21218, USA.

[2]Department of Earth, Ocean and Atmospheric Sciences, University of British Columbia, Vancouver, BC V6T 1Z4, Canada

[3]The Johns Hopkins University Applied Physics Laboratory, Laurel, MD 20723, USA.

[4]Hopkins Extreme Material Institute, The Johns Hopkins University, Baltimore, MD 21218, USA.

ation as our measure of surface roughness. Observations of large craters on Mercury at baselines from 0.5-10 km found higher surface roughness values at the central uplifts, rims, and exteriors of craters, while the crater floors exhibit the lowest roughness values. At baselines less than 10 km, the regions exterior to large craters with diameters > 80 km have the highest surface roughness values. These regions, which include the ejecta and secondary fields, are the main contributors to the increased surface roughness observed in high-crater-density regions. For baselines larger than 10 km, the crater cavity itself is the main contributor to surface roughness. A suite of numerical investigations used the measured surface roughness obtained in the study to model the cumulative effect of adding large craters to a surface. The results indicate that not all of the surface roughness on Mercury is due to fresh large craters, but that impact craters likely contribute to the Hurst exponent from baselines of $0.5 - 1.5$ km and the shape of the deviogram. The simulations show that a surface becomes reaches a steady-state in surface roughness at these baselines studied well before the surface was covered in impact craters.

1. Introduction

Impact craters modify the topography of planetary surfaces. We can quantify the influence of impact craters on the topography of a planetary surface through a statistical measure of the change in detrended vertical topography over a given horizontal scale, surface roughness [e.g., *Shepard et al.*, 2001]. Previous studies have shown that impact craters increase measured surface roughness values [e.g., *Kreslavsky et al.*, 2008; *Rosenburg et al.*, 2011; *Pommerol et al.*, 2012; *Kreslavsky et al.*, 2013; *Yokota et al.*, 2014; *Kreslavsky et al.*, 2014; *Rosenburg et al.*, 2015; *Fa et al.*, 2016; *Kreslavsky and Head*, 2016; *Susorney et al.*, 2017], in this study we focus on investigating how surface roughness characteristics can reflect the physical attributes of an individual impact crater (e.g., the crater floor, ejecta, secondary cratering field) and use a numerical investigation to explore how the regional surface roughness of Mercury is related to large craters (diameters from 25–200 km).

Prior investigations of surface roughness on the Moon and Mercury using many different measures of surface roughness found correlations between regions of high surface roughness values and regions with high crater density [*Kreslavsky et al.*, 2008; *Rosenburg et al.*, 2011; *Pommerol et al.*, 2012; *Kreslavsky et al.*, 2013; *Yokota et al.*, 2014; *Kreslavsky et al.*, 2014; *Rosenburg et al.*, 2015; *Fa et al.*, 2016; *Kreslavsky and Head*, 2016; *Susorney et al.*, 2017] regardless of the measure used. An implicit assumption in interpreting the apparent correlation between crater density and surface roughness is that the crater cavities (the primary topographic depression) are the main factors increasing the measured surface roughness. This assumption has led several authors [e.g., *Rosenburg et al.*,

2011; *Yokota et al.*, 2014; *Fa et al.*, 2016] to propose that surface roughness could be used as a complementary method to crater counts [e.g., *Group*, 1979] to estimate the age of planetary surfaces.

Two studies [*Yokota et al.*, 2014; *Rosenburg et al.*, 2015] investigated in greater detail the relationship between crater density and surface roughness. *Yokota et al.* [2014] measured the surface roughness of the Moon using the measure of median differential slope [*Kreslavsky and Head*, 2000] at horizontal baselines (L) of 0.15-100 km. The study found that the median differential slope at $L = 20$ km correlated well with the cumulative density of craters (N) with diameters greater than 20 km [$N(> 20)$]. A second correlation with $N(> 20)$ was found at $L =$ 6-9 km. The study also used simulated topography with craters modeled as modified cones to test whether they could reproduce the correlation of surface roughness with crater density. The correlation at $L = 20$ km was reproduced, but the simulated topography did not reproduce the correlation at $L =$ 6-9 km. The difference at the smaller baselines (6-9 km) was attributed to the fact that secondary craters and details of ejecta deposits were not incorporated into the model.

Rosenburg et al. [2015] investigated how idealized crater morphology affected topographic power spectral density on the Moon with a simplified model of crater morphology, but did not directly focus on the relationship between crater density and age. The study found the simulated power spectral slope was dependent on the production function of impact craters. The model successfully reproduced the measured power spectra of the lunar surface at baselines of 0.115-1 km.

Several studies have discussed the increase in surface roughness associated with individual impact craters as part of a roughness assessment for broader regions across Mercury

[*Harmon et al.*, 2007; *Neish et al.*, 2013; *Kreslavsky et al.*, 2014; *Fa et al.*, 2016; *Susorney et al.*, 2017]. The centimeter-scale surface roughness of Mercury's craters was approximated using Arecibo radar [*Harmon et al.*, 2007] and an increase in radar brightness (corresponding to higher surface roughness values) was associated with a few large craters (e.g., the crater Hokusai). The centimeter-scale radar brightness was later attributed to large volumes of impact melt in and around craters on Mercury [*Neish et al.*, 2013]. More recent studies of Mercury's surface roughness at baselines comparable to the above-mentioned lunar studies used a range of different surface roughness measurements [*Fa et al.*, 2016; *Kreslavsky et al.*, 2014; *Susorney et al.*, 2017] and data from the MErcury Surface, Space ENvironment, GEochemistry, and Ranging (MESSENGER) mission. All studies noted that regions of higher surface roughness values correlate with regions of higher crater density (the cratered terrain [e.g., *Trask and Guest*, 1975; *Spudis and Guest*, 1988; *Whitten et al.*, 2014]) and regions of lower surface roughness values correlate with regions of lower crater density (the smooth plains [e.g., *Trask and Guest*, 1975; *Spudis and Guest*, 1988; *Denevi et al.*, 2013]). In addition, both *Fa et al.* [2016] and *Susorney et al.* [2017] saw noticeable increases in surface roughness values around individual large craters located in the smooth plains.

In the current study, we build upon previous investigations of the surface roughness of Mercury and focus on the surface roughness created by large impact craters. We limit this study to large craters (diameter $>$ 20 km) since previous studies have observed that the regional surface roughness of Mercury is dominated by such craters [*Kreslavsky et al.*, 2014; *Fa et al.*, 2016; *Susorney et al.*, 2017]. In particular, we want to investigate the source of increased surface roughness around large craters (diameters $>$ 80 km) in the

smooth plains noted in *Fa et al.* [2016]; *Susorney et al.* [2017]. This study is composed of two parts: first, an in-depth analysis of how surface roughness is distributed in and around individual craters (section 2 and 3) and second, a numerical investigation (section 4) where we utilize the measured surface roughness values (from the first part of the study). We use the results of both parts to understand how individual craters modify the surface roughness of Mercury, how collections of craters through time modify surface roughness, and how crater density is related to surface roughness (section 5).

2. Measurement of Surface Roughness

To understand how impact craters affect surface roughness on Mercury, we measured the surface roughness of 17 large craters (see Table S1 for list). We computed the surface roughness of large craters on Mercury using the Mercury Laser Altimeter (MLA) tracks [*Zuber et al.*, 2012]. Using the topography from an individual laser altimetry track to calculate surface roughness is more accurate than using derived gridded topographic products, which typically are generated by binning and smoothing topography to fill in the topography in regions where no altimetry data are present [see discussion in *Glaze et al.*, 2003; *Barnouin-Jha et al.*, 2005; *Robbins and Hynek*, 2013]. Because MLA tracks are concentrated in Mercury's northern hemisphere this investigation uses craters in the northern hemisphere.

We used root-mean-square (RMS) deviation as our measure of surface roughness; RMS deviation is the RMS change in detrended height over a given horizontal scale. We choose to use RMS deviation rather than other measures of surface roughness [e.g., *Kreslavsky et al.*, 2013] for several reasons. First, RMS deviation is commonly used in planetary radar and laser altimetry surface roughness studies [e.g., *Rosenburg et al.*, 2011; *Orosei*, 2003;

Fa et al., 2016] and terrestrial surface roughness studies [e.g., *Mark and Aronson*, 1984]. Second RMS deviation is related to the proposed self-affine behavior of natural surface s [e.g., *Turcotte*, 1997]. If RMS deviation is plotted against the baselines in a log-log plot and the resulting plot is linear in log-log space a Hurst exponent can be fit to the data. A single diagnostic Hurst exponent for a surface has been postulated to indicate that its topography is the result of a single geologic process without any characteristic scale [e.g., *Shepard et al.*, 2001]. Additionally, previous studies exploring the relationship between surface roughness and crater densities used other measures of surface roughness rather than RMS deviation (median differential slope, [*Yokota et al.*, 2014] and topographic power spectra [*Rosenburg et al.*, 2015]). This permits us to explore the relationship of a different surface roughness parameter and crater density.

Larger regional maps of RMS deviation were presented in *Susorney et al.* [2017], and were used to understand the relative contribution of volcanism, tectonics, and impact cratering to regional surface roughness. In this section, we will briefly review RMS deviation and its relationship to the self-affine nature of topography and how we filtered MLA data before measuring RMS deviation. We then explain how surface roughness maps were produced and how radial plots of surface roughness around large craters were generated.

2.1. Measurements from MLA data

The surface roughness was measured at baselines of 0.5-250 km with the smallest baseline being constrained by the spacing between individual returns along an MLA track, which vary from 0.3-0.7 km. Individual MLA points were evaluated for each baseline investigated to check that the spacing between MLA points within five times the baseline on either side of the point was less than the baseline investigated [see *Susorney et al.*,

2017]. If the MLA point had appropriate spacing, adjacent MLA points within five times the baseline were interpolated to generate a spacing equivalent to the baseline being measured. In *Susorney et al.* [2017] this methodology (see Fig. 3 in *Susorney et al.* [2017]) was compared to topography that was not interpolated and no statistical difference in the resulting surface roughness values was found. Then, ten times the baseline of interest was detrended to remove broad-scale slopes (five times on either side of the MLA point, following recommendations in *Shepard et al.* [2001]). The difference in height one baseline up and one down from the MLA point was then measured. The change in height $[\Delta h(L)_i]$ was then used to calculate $\nu(L)$ using Eqn. (1).

2.2. RMS Deviation

RMS deviation, $\nu(L)$, is the change in detrended topographic height, h, over a given horizontal baseline, L, and is defined by

$$\nu(L) = \left\{ \frac{1}{n} \sum_{i=1}^{n} [\Delta h(L)_i]^2 \right\}^{\frac{1}{2}}, \tag{1}$$

where $\Delta h(L)_i$ is the change in height and i is the number of Δh used to calculate RMS deviation. RMS deviation is related to the Hurst exponent, H, which describes how the surface roughness changes with increasing baseline by

$$\nu(L) = \nu_o L^H, \tag{2}$$

where ν_o is the RMS deviation at the unit scale. If the surface has self-affine-behavior a straight line can be fit to the log of L versus the log of $\nu(L)$ and the resulting exponent of the fit to the line is H [*Turcotte*, 1997]. It has been postulated that when a single H exists for a surface then a single geologic process without any characteristic scale might control the observed topography [e.g., *Shepard et al.*, 2001]. When referring to the results of this

study surface roughness and RMS deviation are used interchangeably. RMS deviation was calculated from the data in two ways. For the maps, the Δh was gridded across the surface into grid sizes twice the baseline of interest, then RMS deviation was calculated for each grid point. For the radial plots, the Δh were sorted into radial 1 km bins around the crater and if more than 100 Δh were found in each bin RMS deviation was calculated. We required at least 100 Δh to be in each bin because RMS deviation is unstable below this threshold for Mercury [*Susorney et al.*, 2017].

2.3. Maps of Surface Roughness

To understand how the surface roughness is distributed in and around large craters on Mercury, we generated maps of surface roughness centered on large craters using the Generic Mapping Tools (GMT, http://gmt.soest.hawaii.edu, *Wessel et al.* [2013]). Maps were gridded at twice the baseline at which the surface roughness was computed to avoid smearing. This, for example, meant that a map at $L = 1$ km would be gridded at 2 km. A continuous curvature spline fit was added to ease presentation of data [*Smith and Wessel*, 1990]. Maps without spline fits were consulted to check that no artifacts were introduced by these fits. Maps were used for qualitative comparisons only since due to sparse MLA coverage the required 100 Δh were not in each gridded bin.

2.4. Surface Roughness Radial Analysis

In addition to the maps of surface roughness, we also calculated radial profiles of surface roughness around the large craters. For each crater, we sorted all measurements of Δh into their radial distance from the center of the crater. We then calculated the RMS

deviation for 1-km-wide bins (e.g. the RMS deviation of all Δh that were 0-1 and then 1-2 km away from the center of the crater).

3. Surface Roughness Observations of Large Craters

In this section, we use the roughness data products described above to assess the surface roughness in and around large craters on Mercury and how the distribution of surface roughness changes with crater diameter. We first look at large craters with diameters (d) greater than 50 km, then at large craters with $d < 50$ km, and then at an unusual crater, Hokusai. Finally, we use the crater Abedin as a case study for studying the spatial relationship of specific crater attributes and the measured surface roughness for craters with diameters larger than 50 km. In Fig. 1 you can see the locations of craters studied on the surface of Mercury.

3.1. Craters with diameters over 50 km, $d > 50$ km

The surface roughness maps of five relatively fresh craters at $L = 1$ km (two of which are on the same map) are shown in Fig. 2, the first four of these craters have diameters larger than 50 km. All five of these craters lie in the smooth plains (region of lower crater density compared with the heavily cratered terrain) where the pre-existing topography is qualitatively smooth and is not an important contributor to the surface roughness measured at and around these craters [*Kreslavsky et al.*, 2014; *Fa et al.*, 2016; *Susorney et al.*, 2017]. This study will focus on the surface roughness of fresh craters where the surface roughness has been minimally affected by degradation. The five craters in Fig. 2 are considered fresh and minimally degraded [*Susorney et al.*, 2016] and all the craters

measured in this study do not appear to have their surface roughness strongly affected by crater degradation.

The craters Abedin (Fig. 2(a-c)), Stieglitz (the larger crater in Fig. 2(d-f)), and Gaudi (the medium-sized crater in Fig. 2(d-f)) all show surface roughness distributions typical of craters with diameters over 50 km on Mercury. They have smaller surface roughness values in the crater floor, greater values near the central peak and rim, and a large region of high surface roughness values beyond the crater rim. For the 1 km baseline, the range in surface roughness values is from 0.001–0.25 km. This region of enhanced surface roughness exterior to the crater rim is not easily attributed to a single aspect of crater morphology and occurs over a region that includes both the continuous ejecta and the secondary crater fields.

Radial plots of the $L = 1$ km surface roughness of Abedin, Gaudi, and Stieglitz are shown in Figure 3(a-c) and are also plotted against the radial MLA topography measured in the same 1-km radial bins. The radial plots show the same pattern as the maps, with increased surface roughness values around the central uplift (peak or ring) and the crater rim; the crater floors have decreased surface roughness.

The radial surface roughness plots of Abedin and Stieglitz show a decrease immediately exterior to the crater rim, but then an increase to form a qualitative local maximum [Fig. 3(a)]. We identified this qualitative local maximum in surface roughness through a visual inspection of the crater plots (see Figs. S1 and S2). Six of the 17 crater measured exhibit this qualitative local maximum and all of the craters that had the qualitative local maximum are larger than 100-km in diameter. In Fig. 3(f) we plot the diameter of the crater studied versus whether it had a qualitative local maximum outside of the crater

rim. When we produced radial plots of these same craters at $L = 0.5$ km (Figs. S3-S5), we still observe a qualitative local maximum for those craters where it was previously identified (for the $L = 1$ km), but also observed local maxima for different craters that are 80-100 km diameters indicating that the presence of a qualitative local maximum in the surface roughness exterior to the crater scales with crater diameter and the horizontal scale over which surface roughness is measured.

Plots of the radial profile of surface roughness for the crater Abedin at $L = 0.5$, 5, 20, and 100 km are shown in Figure 4. The $L = 0.5$ km radial plot shows the same general qualitative local maximum as $L = 1$ km, but it disappears in the $L = 5$ km and larger baseline radial plots. In the $L = 20$ and 100 km radial plots, the surface roughness does not have high surface roughness values associated the central uplift and rim; instead, there is just a single increase in surface roughness associated with the crater cavity.

In the smooth plains only two craters with diameters over 50 km have overlapping ejecta/secondary fields, Gaudi and Stieglitz. In the map of Gaudi and Stieglitz [Fig. 2(d-f))], the regions of increased roughness values surrounding the craters overlap, but the measured roughness values are not additive when the ejecta and secondary fields are superposed. In addition, the enhanced surface roughness exterior to the crater overprints the surface roughness from pre-existing smaller craters. The surface roughness did not co-add in any of the baselines investigated. This supports observations in images of the surface of Mercury, that show overlapping ejecta combining to produce a similar visual texture *Whitten et al.* [2014]. Additionally, the radial plots of Gaudi and Stieglitz (Fig. 2(b) and (c) show similar surface roughness values to each other and are not higher than the surface roughness values of the crater Abedin (Fig. 2(a)). If the surface roughness was

co-adding we may expect the surface roughness of Gaudi and Stieglitz to be higher than other craters that are not adjacent to other fresh large craters. Also, a radial analysis of the surface roughness of Stieglitz broken into four quadrants (Fig. S6) around the crater show no differences in the surface roughness as would be expected in the northern two quadrants if the surface roughness was co-adding with the surface roughness of Gaudi.

3.2. Craters with diameters under 50 km

Craters with diameters under 50 km such as Egonu (Fig. 2(j-l), $d = 25.0$ km) have surface roughness attributes similar to craters over 50 km in diameter within the crater cavity. Egonu has increased roughness values at its rim and central peak, and reduced values on the crater floor. However, Egonu does not possess a region of increased surface roughness exterior to the crater rim. The radial plot of Egonu [Fig. 3(e)] confirms this pattern: interior to the crater rim, the measured roughness is similar to craters over 50 km in diameter, but no qualitative local maximum is found exterior to the crater rim, consistent with the diameter and baseline dependency noted before. Three additional craters (Grotell, Riveria, and Martial, see Figs. S1 and S2) with diameters near or under 50 km show the same pattern in surface roughness as Egonu.

3.3. Hokusai, an unusual large crater on Mercury

Hokusai (Fig. 2(g-i) and Fig. 3(d)) is a notable exception to the pattern outlined above for craters with diameters greater than 50 km in the smooth plains. The map of the surface roughness of Hokusai has a smaller region of enhanced surface roughness values compared to other craters over 50 km in diameter (e.g., Abedin). Previous studies of Hokusai have noted extensive melt and unusual ejecta [rampart like structures, *Xiao and*

Komatsu, 2013; *Barnouin et al.*, 2015; *Xiao et al.*, 2016]. Arecibo radar data noted a region of elevated roughness values around Hokusai [*Harmon et al.*, 2007] likely due to Hokusai having extensive melt, which is rough in radar-scale (S-band) surface roughness [*Neish et al.*, 2013] due to the centimeter-scale structure and smooth at $L = 1$ km surface roughness since melt will infill 'rougher' topography. Additionally, *Xiao et al.* [2014] reported a lower density of secondary craters surrounding Hokusai. Impact melt exterior to the crater rim would explain the lower $L = 1$ km surface roughness values since melt would infill the regions of higher surface roughness values observed in other craters over 50 km in diameter. It is also possible that extensive melt in the ejecta reduced the strength of blocks in the ejecta and thus the number of secondary craters around Hokusai [e.g., *Schultz and Singer*, 1980]. The lower density of secondary craters could result in lower surface roughness values exterior to the crater rim. Hokusai is also likely one of the youngest craters on the planet due to its degradation state [*Susorney et al.*, 2016], but there are also very fresh craters on the surface that do not display the same amount of melt as Hokusai. Additionally, the MLA coverage around Hokusai is not as dense as the coverage around Abedin, but in the radial surface roughness plots had sufficient Δh present to calculate RMS deviation.

3.4. Abedin

To investigate the origin of the qualitative local maximum in the $L = 1$ km surface roughness maps and profiles, we investigate in detail the relatively fresh crater Abedin. In particular, we focus on whether secondaries or ejecta is the source of elevated surface roughness exterior to the crater,

3.4.1. Geologic map of Abedin

The geology of Abedin was mapped (Fig. 5) using a 250 m/pixel Mercury Dual Imaging System mosaic. The mapping was performed on a sphere in the Small Body Mapping Tool (SBMT) [e.g., *Kahn et al.*, 2011]. We focused on identifying the radial limits of the ejecta, crater floor, central peak, and rim. In Fig. 6 we marked the radial extent of the crater floor, ejecta, and secondary fields on a radial surface roughness plot. The qualitative local maximum straddles the continuous ejecta and secondary fields.

3.4.2. Density of secondary craters around Abedin

To investigate whether secondary craters are correlated with the qualitative local maximum exterior to the crater rim, we compared secondary crater density to surface roughness by mapping all secondary craters (we assumed all small craters, diameters under 10 km, that were outside of Abedin's rim were secondaries for this part of the study) over 1 km in diameter within six crater radii of the center of Abedin. Over 7000 secondary craters >1 km in diameter were identified in the Small Body Mapping Tool [*Kahn et al.*, 2011] using the same 250 m/pixel Mercury Dual Imaging System mosaic. In Figure 7 the radial density (in 1 km bins) of secondary craters (1-10 km in diameter) is plotted with the $L =$ 1 km surface roughness of Abedin against the distance from the center of Abedin. We calculated the density of secondary craters in 1 km radial bins and took the total number of craters in the annulus and divided by the area of the annulus. The maximum in secondary crater density is farther from the crater center than the local surface roughness maximum. This observation implies that secondary craters are not the only source of the qualitative local maximum. A mixture of the continuous ejecta and secondary craters is likely the source of this qualitative local maximum, given that it is straddling the transition between these two regions.

4. Numerical Investigations

We used a numerical investigation to understand how the formation of multiple impact craters influences the regional surface roughness of Mercury. These simulations did not try to re-create the actual topography of a cratered surface [e.g., *Gaskell*, 1993; *Richardson*, 2009; *Yang et al.*, 2013; *Rosenburg et al.*, 2015], which must make assumptions of the topography created by craters. Instead, we used the measured surface roughness values in and around large craters on Mercury (the results from section 3) to test whether we can re-create aspects of the regional surface roughness observed on Mercury in the smooth plains and cratered terrains using fresh large craters alone.

4.1. Investigation set-up and assumptions

In this investigation, we used the measured radial distribution of surface roughness (at all baselines measured of 0.5–250 km) out to four crater radii from the center of five large craters ranging in diameter from 25–100 km. Details about the five craters selected are in Table 1. The range of crater diameters were chosen to match the five bin sizes used in crater counts by *Ostrach et al.* [2015], who investigated the crater size-frequency distribution on the smooth plains and the cratered terrains of Mercury. An artificial 1000-km-by-1000-km surface was generated with an initial surface roughness of 0.0 km. Changing this initial value to match background (non-large cratered) surface roughness, for example, was found to have no influence on the final outcome of the roughness computed for the artificial surface (Fig. S7). The Δh from the radial distribution of surface roughness of the five craters were then added to random locations on the surface and RMS deviation was calculated from this. The location of each crater was based on the

size-frequency measured by *Ostrach et al.* [2015] for either the smooth plains or cratered terrain [see Fig. 8(a) and (d)].

We performed more computationally expensive simulations using a 2000-km-by-2000-km surface measured in the same manner above and the 2000-km-by-2000-km surface where we only measured the center 1000-km-by-1000-km surface to check for any boundary effects. The results of both of these simulations are found in the supplementary information (Figure S8 and S9) and the Hurst exponent and shape of the deviogram measured from these two simulations are not different from the simulations run in the original 1000-km-by-1000-km configuration.

When a new crater was added to the surface, its roughness overprinted any pre-existing surface roughness. This assumption prevented us from introducing additional complexity to our numerical simulation. Additionally, observations of Gaudi and Stieglitz showed that overlapping regions of elevated surface roughness did not co-add and that there surface roughness overprinted surface roughness due to an older crater in the region.

Craters were added to the surface until the simulated size-frequency distribution on the surface matched either the smooth plains or cratered terrain as measured by *Ostrach et al.* [2015]. The surface roughness of the complete 1000-km-by-1000-km surface was recalculated after each crater was added (Fig. 8(c) and (f)). We also calculated the Hurst exponent from baselines of 0.5-1.5 km, the same baselines found to have self-affine-like behavior in *Susorney et al.* [2017].

4.2. Results of the numerical investigation

Figs. 9 and 8 show the simulated surface roughness, crater-size-frequency, and deviogram (RMS deviation versus baseline) of simulated regions where the final crater den-

sities match the smooth plains and cratered terrain, respectively. Fig. 10 compares the final deviogram for 30 runs for the simulated smooth plains and cratered terrain to the measured surface roughness of the two regions on Mercury obtained in *Susorney et al.* [2017].

At baselines of 0.5–1.5 km, the simulated deviograms are approximately linear resulting in Hurst exponents of 0.98 ± 0.01 and 0.99 ± 0.00 for the smooth plains and cratered terrains, respectively. We choose the baselines of 0.5–1.5 to match the baselines a Hurst exponent was fit to in [*Susorney et al.*, 2017] since we compared the results of the simulation to the results of that paper. The values of the Hurst exponent are the mean of thirty separate simulations and the uncertainties are one standard deviation of the thirty runs. These Hurst exponents are larger than the measured H of the cratered terrain (0.95) and smooth plains (0.88) for the same baselines [*Susorney et al.*, 2017]. *Fa et al.* [2016] measured different Hurst exponents for the smooth plains (0.60) and cratered terrain (0.80) of Mercury, but these were measured over a broader range of baselines (L = 0.4–4.2 km). There could be many reasons for the larger Hurst exponent in our models compared to observations, a larger Hurst exponent means that topography is larger for longer baseline compared to a small Hurst exponent. This larger increase in topography could be due to the lack of degradation in our models or the lack of small craters.

The shape of the deviogram at $L < 40$ km is reproduced in the numerical investigation. However, the simulated and measured deviograms do not overlap each other, with the simulated deviogram having a lower overall surface roughness than the measured deviogram at all baselines. A second measured deviogram of the smooth plains from measured surface roughness values is also plotted in Fig. 10 (Smooth Plains 2). This second deviogram

of the smooth plains was measured away from the smooth plains unit boundary, where boundary effects from the cratered terrain can influence the surface roughness (see *Susorney et al.* [2017]). In this second deviogram, the measured deviogram and simulated deviogram are closer in agreement, with a bend in the surface roughness around $L =$ 30 km being reproduced although the measured surface roughness of Smooth Plains 2 is larger than the simulated surface roughness of the smooth plains. The lower surface roughness values in our simulation compared to measured surface roughness on Mercury is likely due to a combination of the lack of simple craters, tectonics, and large basins [*Fa et al.*, 2016; *Susorney et al.*, 2017] and the complete overprinting of the surface roughness of pre-existing craters in our simulations. In particular, the lack of degradation and complete overprinting of pre-exsisting surface roughness is likely not an accurate representation of the evolution of highly cratered surfaces however, it is difficult to tease apart how the surface roughness of many impact craters interact in heavily cratered surfaces. The role of smaller diameter craters may be important in driving the evolution of surface roughness as small diameter craters are an important aspect in crater equilibrium on a surface *Xiao and Werner* [2015].

5. Discussion

In this section, we use both observations of the surface and numerical simulations to understand how large craters produce and modify surface roughness on Mercury. We also assess any relationship between measured surface roughness produced by large craters and crater density.

5.1. Individual large craters

Our results indicate that the distribution of surface roughness around large craters on Mercury at smaller baselines (L < 10 km) is well correlated with the morphology of the crater. The largest regional contributor to surface roughness is the area exterior to the crater rim. A few large ($d > 80$ km) large craters can completely dominate the local surface roughness of terrain with a few impact craters (e.g., the smooth plains on Mercury). This finding supports observations by *Fa et al.* [2016]; *Susorney et al.* [2017] that individual large craters appear to dominate the surface roughness at smaller baselines. Simulations measuring the surface roughness by *Yokota et al.* [2014] produced by simulated craters (modeled as modified cones) didn't reproduce the local maxima in roughness at baselines of 6–9 km that was associated with impact craters. The authors hypothesized it was due to the lack of realistic ejecta and secondary craters in their simulations. Our observation of the importance of ejecta and secondary fields for surface roughness at baselines under 10 km support the authors' hypothesis.

5.2. Interaction of multiple impact craters

Our observations of the surface roughness of the craters Gaudi and Stieglitz with their overlapping ejecta and secondary fields show that the surface roughness of the exterior of craters does not co-add, but simply overprints. Observations of the cratered terrain on Mercury noted that the qualitative rough texture of the cratered terrain is created by overlapping ejecta blankets [*Whitten et al.*, 2014]. This qualitative observation is similar to our observation of the importance of the region exterior to craters (in particular when these regions overlap) to increasing the surface roughness of an entire region at small baselines ($L < 10$ km).

The numerical investigation yielded H values for the simulated smooth plains and cratered terrain of 0.998+/-0.01 and 0.99+/-0.00 are similar to the measured H of the cratered terrain (0.95 $\pm$ 0.01) at the same baselines and the lunar highlands where H = 0.95 for L = 0.017-2.7. The similarity among all these Hurst exponents may support the hypothesis that a Hurst exponent is indicative of a single geologic process without a diagnostic scale controlling surface roughness at these scales [e.g., *Shepard et al.*, 2001; *Rosenburg et al.*, 2011], in this case, impact cratering.

5.3. Surface roughness and crater density

Previous studies have proposed that surface roughness can be used to estimate surface age since regions with higher surface roughness values usually have higher crater densities [e.g., *Yokota et al.*, 2014]. Here, we can use our results to investigate how surface roughness changes with increasing crater density. Fig. 11 shows our surface roughness values for the entire simulated region after increasing numbers of large craters are emplaced on a region for the cratered terrain simulation in Section 5 (for L = 0.5, 1, 5, 10, 40 km). The gray region represents the one standard deviation of 30 runs. The plot indicates that after 15 craters are emplaced, the surface roughness for L = 0.5 and 1 km does not increase but remains constant. When the surface roughness does not change with increasing number of craters we believe the region is in "steady-state surface roughness". The surface roughness at 5 and 10 km baselines reaches a steady-state after $\sim$30 craters are added. The L = 40 km surface roughness reaches a steady-state after $\sim$80 craters are added, but the uncertainty is large. Surfaces dominated by large craters reach a surface roughness steady-state before the surface is completely covered in craters at the baselines investigated.

At $L < 10$ km, the surface roughness measured is dominated by the region exterior to the crater rim and covers a large surface area. It should not, therefore, be surprising that at these baselines the roughness reaches a steady-state after only a few craters form. This result shows that it is not possible to relate the surface roughness at smaller baselines to crater density/surface age on Mercury for terrains similar to the cratered terrain. At $L >$ 10 km, the surface roughness generated by a single crater is dominated by that crater's cavity. Thus, for these longer baselines, the time required to reach surface roughness steady-state is longer. This is consistent with the results of *Yokota et al.* [2014], who found, with their idealized crater shapes and cavities as the main source of surface roughness in the simulations, that a correlation existed between surface roughness for L between 20-30 km and crater density N(>20km). In our investigation, we find that for baselines of 20–40 km it is difficult to identify a simple relationship between crater density and surface roughness alone since there is some variation in this relationship, as seen in Fig. 11 where variation between simulations for these larger baselines is quite large. While we can not rule out using the surface roughness at larger baselines as a proxy for crater density/surface age, the variation in the relationship would always be a larger source of uncertainty in any result.

6. Conclusions

For many planetary bodies, impact craters are the dominant source of surface roughness. In this paper, we have investigated how large craters influence the surface roughness of Mercury. The main results of our study are:

1. For baselines $L < 10$ km, large craters on Mercury have larger surface roughness values at the crater rim and central peak and lower values on the crater floor. The region

exterior to the crater rim is the largest areal source of surface roughness for these baselines. Exterior to fresh large craters (diameters > 80 km) there is a qualitative local maximum in surface roughness that occurs in a region that includes both continuous ejecta and secondary fields.

2. When multiple large impact craters occur near each other the resulting region of elevated surface roughness exterior to the crater rims do not co-add, but instead merge and results in a region reaching surface roughness steady-state rapidly as these regions of high surface roughness merge.

3. For $L > 10$ km, the surface roughness is primarily due to the crater's cavity (the decrease in elevation from the rim to the crater floor).

4. The large crater Hokusai has a smaller region of increased surface roughness values exterior to the crater rim as compared to similarly size fresh large craters. This reduction in surface roughness values is likely due to the large amount of impact melt in and around Hokusai and fewer number of secondary craters.

5. A numerical investigation into whether large craters alone can produce the surface roughness measured on Mercury found that the majority of the surface roughness of the smooth plains and cratered terrain can be attributed to large craters, but not all. The Hurst exponent from the numerical investigation for both the smooth plains and cratered terrain is similar to the Hurst exponent of Mercury's cratered terrain and the lunar highlands.

6. The relationship between surface roughness and crater density varies based on baseline investigated. At $L < 10$ km, the region exterior to the crater dominates surface roughness and results in a surface reaching surface roughness steady-state after only a

few craters have been added to the surface. At $L > 10$ km surface roughness appears to be linked with the crater cavity itself and could be a better proxy for age, although, there is some variation between identical numerical simulations.

Acknowledgments.

We would like to thank Drs. Hauck and Fa for editorial handling and Drs. Kreslavsky, Cao, and an anonymous reviewer for their comments that improved the paper. Support was provided by the Johns Hopkins University Applied Physics Laboratory Graduate Student Fellowship Program for H.C.M.S., and the Johns Hopkins University Applied Physics Laboratory Hafstad Fellowship program for O.S.B. We would like to acknowledge the Small Body Mapping Tool developed by the Johns Hopkins University Applied Physics Laboratory for geologic mapping in this study. Finally, we thank the scientists and engineers of the MESSENGER mission for the MLA dataset.

Data used in the creation of this paper will be released on Zenobo upon publication.

References

Barnouin, O. S., C. M. Ernst, and H. C. M. Susorney (2015), The Remarkable Hokusai Crater, Mercury, *46th Lunar and Planetary Science Conference*, *46*, 2672.

Barnouin-Jha, O. S., S. Baloga, and L. Glaze (2005), Comparing landslides to fluidized crater ejecta on Mars, *Journal of Geophysical Research*, *110*(E), 4010.

Denevi, B. W., C. M. Ernst, H. M. Meyer, M. S. Robinson, S. L. Murchie, J. L. Whitten, J. W. Head, T. R. Watters, S. C. Solomon, L. R. Ostrach, C. R. Chapman, P. K. Byrne, C. Klimczak, and P. N. Peplowski (2013), The distribution and origin of smooth plains on Mercury, *Journal of Geophysical Research: Planets*, *118*(5), 891–907.

Fa, W., Y. Cai, Z. Xiao, and W. Tian (2016), Topographic roughness of the northern high latitudes of Mercury from MESSENGER Laser Altimeter data, *Geophysical Research Letters*, p. doi:10.1002/2016GL068120.

Gaskell, R. W. (1993), Martian Surface Simulations, *Journal of Geophysical Research*, *98*(E6), 11,099–11,103.

Glaze, L. S., S. M. Baloga, and E. R. Stofan (2003), A methodology for constraining lava flow rheologies with MOLA, *Icarus*, *165*(1), 26–33.

Group, C. A. T. W. (1979), Standard techniques for presentation and analysis of crater size-frequency data, *Icarus*, *37*, 467–474.

Harmon, J. K., M. A. Slade, B. J. Butler, J. W. I. Head, M. S. Rice, and D. B. Campbell (2007), Mercury: Radar images of the equatorial and midlatitude zones, *Icarus*, *187*(2), 374–405.

Kahn, E. G., O. S. Barnouin, D. L. Buczkowski, C. M. Ernst, N. Izenberg, S. Murchie, and L. M. Prockter (2011), A Tool for the Visualization of Small Body Data, *42nd Lunar and Planetary Science Conference*, *42*, 1618–.

Kreslavsky, M. A., and J. W. Head (2000), Kilometer-scale roughness of Mars: Results from MOLA data analysis, *Journal of Geophysical Research: Planets (1991–2012)*, *105*(E11), 26,695–26,711.

Kreslavsky, M. A., and J. W. Head (2016), The steepest slopes on the Moon from Lunar Orbiter Laser Altimeter (LOLA) Data: Spatial Distribution and Correlation with Geologic Features, *Icarus*, *273*, 329–336.

Kreslavsky, M. A., J. W. Head, and J. K. Harmon (2008), Large-Scale Topographic Roughness of Terrestrial Planets: A Comparison, *39th Lunar and Planetary Science*

514 *Conference*, *39*, 1472.

515 Kreslavsky, M. A., J. W. Head, G. A. Neumann, M. A. Rosenburg, O. Aharonson, D. E.
516 Smith, and M. T. Zuber (2013), Lunar topographic roughness maps from Lunar Orbiter
517 Laser Altimeter (LOLA) data: Scale dependence and correlation with geologic features
518 and units, *Icarus*, *226*(1), 52–66.

519 Kreslavsky, M. A., J. W. Head, and G. A. Neumann (2014), Kilometer-scale topographic
520 roughness of Mercury: Correlation with geologic features and units, *Geophysical Re-*
521 *search Letters*, *41*, 1–7.

522 Mark, D. M., and P. B. Aronson (1984), Scale-dependent fractal dimensions of topographic
523 surfaces: An empirical investigation, with applications in geomorphology and computer
524 mapping, *Mathematical geology*, *16*(7), 671–683.

525 Neish, C. D., D. T. Blewett, J. K. Harmon, E. I. Coman, J. T. S. Cahill, and C. M.
526 Ernst (2013), A comparison of rayed craters on the Moon and Mercury, *Journal of*
527 *Geophysical Research: Planets*, *118*(10), 2247–2261.

528 Orosei, R. (2003), Self-affine behavior of Martian topography at kilometer scale from Mars
529 Orbiter Laser Altimeter data, *Journal of Geophysical Research*, *108*(E4), 8023.

530 Ostrach, L. R., M. S. Robinson, J. L. Whitten, C. I. Fassett, R. G. Strom, J. W. Head,
531 and S. C. Solomon (2015), Extent, age, and resurfacing history of the northern smooth
532 plains on Mercury from MESSENGER observations, *Icarus*, *250*, 602–622.

533 Pommerol, A., S. Chakraborty, and N. Thomas (2012), Comparative study of the surface
534 roughness of the Moon, Mars and Mercury, *Planetary and Space Science*, *73*(1), 287–
535 293.

Richardson, J. E. (2009), Cratering saturation and equilibrium: A new model looks at an old problem, *Icarus*, *204*(2), 697–715.

Robbins, S. J., and B. M. Hynek (2013), Utility of laser altimeter and stereoscopic terrain models: Application to Martian craters, *Planetary and Space Science*, *86*, 57–65.

Rosenburg, M. A., O. Aharonson, J. W. Head, M. A. Kreslavsky, E. Mazarico, G. A. Neumann, D. E. Smith, M. H. Torrence, and M. T. Zuber (2011), Global surface slopes and roughness of the Moon from the Lunar Orbiter Laser Altimeter, *Journal of Geophysical Research*, *116*(E2), E02,001.

Rosenburg, M. A., O. Aharonson, and R. Sari (2015), Topographic power spectra of cratered terrains: Theory and application to the Moon, *Journal of Geophysical Research: Planets*, *120*(2), 177–194.

Schultz, P. H., and J. Singer (1980), A comparison of secondary craters on the Moon, Mercury, and Mars, *Lunar and Planetary Science Conference*.

Shepard, M. K., B. A. Campbell, M. H. Bulmer, T. G. Farr, L. R. Gaddis, and J. J. Plaut (2001), The roughness of natural terrain: A planetary and remote sensing perspective, *Journal of Geophysical Research*, *106*(E), 32,777–32,796.

Smith, W. H., and P. Wessel (1990), Gridding with Continuous Curvature Splines in Tension, *Geophysics*, *55*(3), 293–305.

Spudis, P. D., and J. E. Guest (1988), Stratigraphy and geologic history of Mercury, *IN: Mercury (A89-43751 19-91). Tucson*, pp. 118–164.

Susorney, H., O. Barnouin, C. Ernst, and P. Byrne (2017), Surface Roughness of Mercury from MESSENGER, *Journal of Geophysical Research - Planets*, *in-press*, NA.

558 Susorney, H. C. M., O. S. Barnouin, C. M. Ernst, and C. L. Johnson (2016), Morphometry
559 of impact craters on Mercury from MESSENGER altimetry and imaging, *Icarus*, *271*,
560 180–193.

561 Trask, N. J., and J. E. Guest (1975), Preliminary geologic terrain map of Mercury, *Journal*
562 *of Geophysical Research: Planets*, *80*(17), 2461–2477.

563 Turcotte, D. L. (1997), *Fractals and Chaos in Geology and Geophysics*, Cambridge Uni-
564 versity, Cornell University, New York.

565 Wessel, P., W. H. F. Smith, R. Scharroo, J. Luis, and F. Wobbe (2013), Generic Mapping
566 Tools: Improved Version Released, *Eos*, *94*(4), 409–410.

567 Whitten, J. L., J. W. Head, B. W. Denevi, and S. C. Solomon (2014), Intercrater plains on
568 Mercury: Insights into unit definition, characterization, and origin from MESSENGER
569 datasets, *Icarus*, *241*(C), 97–113.

570 Xiao, Z., and G. Komatsu (2013), Planetary and Space Science, *Planetary and Space*
571 *Science*, *82-83*(C), 62–78.

572 Xiao, Z., and S. C. Werner (2015), Size-frequency distribution of crater populations in
573 equilibrium on the Moon, *Journal of Geophysical Research: Planets*, *120*(12), 2277–
574 2292.

575 Xiao, Z., R. G. Strom, C. R. Chapman, J. W. Head, C. Klimczak, L. R. Ostrach, J. Hel-
576 bert, and P. D'Incecco (2014), Comparisons of fresh complex impact craters on Mer-
577 cury and the Moon: Implications for controlling factors in impact excavation processes,
578 *Icarus*, *228*, 260–275.

579 Xiao, Z., N. C. Prieur, and S. C. Werner (2016), The self-secondary crater population of
580 the Hokusai crater on Mercury, *Geophysical Research Letters*, *43*(14), 7424–7432.

Yang, D., M. T. Zuber, J. W. Head, and S. C. Solomon (2013), Distribution of Topographic Slope and Roughness in Mercury's Northern Hemisphere, *44th Lunar and Planetary Science Conference*, *44*, 2347.

Yokota, Y., K. Gwinner, J. Oberst, J. Haruyama, T. Matsunaga, T. Morota, H. Noda, H. Araki, M. Ohtake, S. Yamamoto, P. Gläser, Y. Ishihara, C. Honda, N. Hirata, and H. Demura (2014), Variation of the lunar highland surface roughness at baseline 0.15-100 km and the relationship to relative age, *Geophysical Research Letters*, *41*(5), 1444–1451.

Zuber, M. T., D. E. Smith, R. J. Phillips, S. C. Solomon, G. A. Neumann, S. A. Hauck II, S. J. Peale, O. S. Barnouin, J. W. Head, C. L. Johnson, F. G. Lemoine, E. Mazarico, X. Sun, M. H. Torrence, A. M. Freed, C. Klimczak, J.-L. Margot, J. Oberst, M. E. Perry, R. L. McNutt Jr, J. A. Balcerski, N. Michel, M. J. Talpe, and D. Yang (2012), Topography of the Northern Hemisphere of Mercury from MESSENGER Laser Altimetry, *Science*, *336*(6078), 217–220.

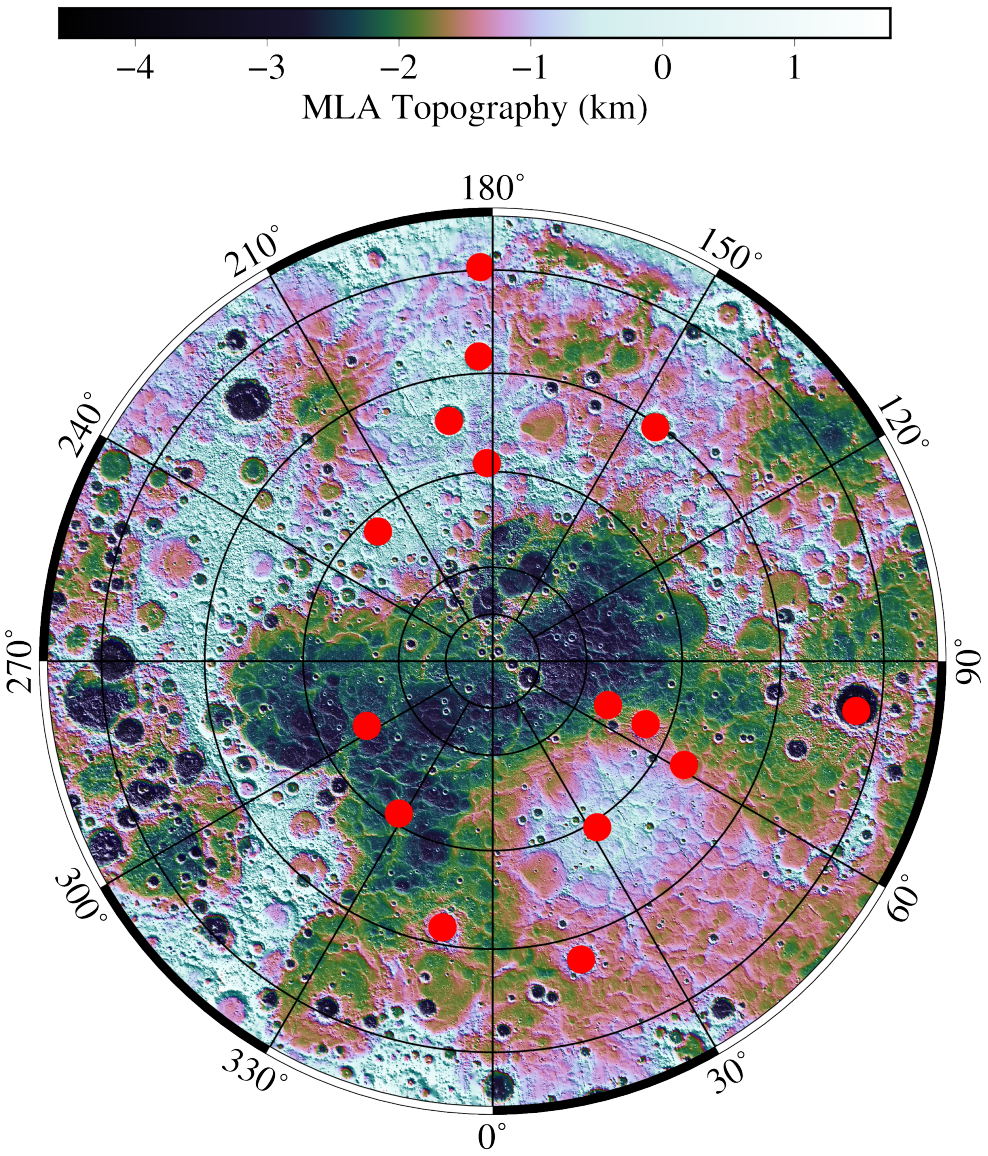

Figure 1. MLA topography map in a polar sterographic projection starting at 45° N with 16 of the 17 craters used in this study plotted as red dots in their respected location on the surface of Mercury. The crater Ahmad Baba is not plotted since its latitude is below 45° N.

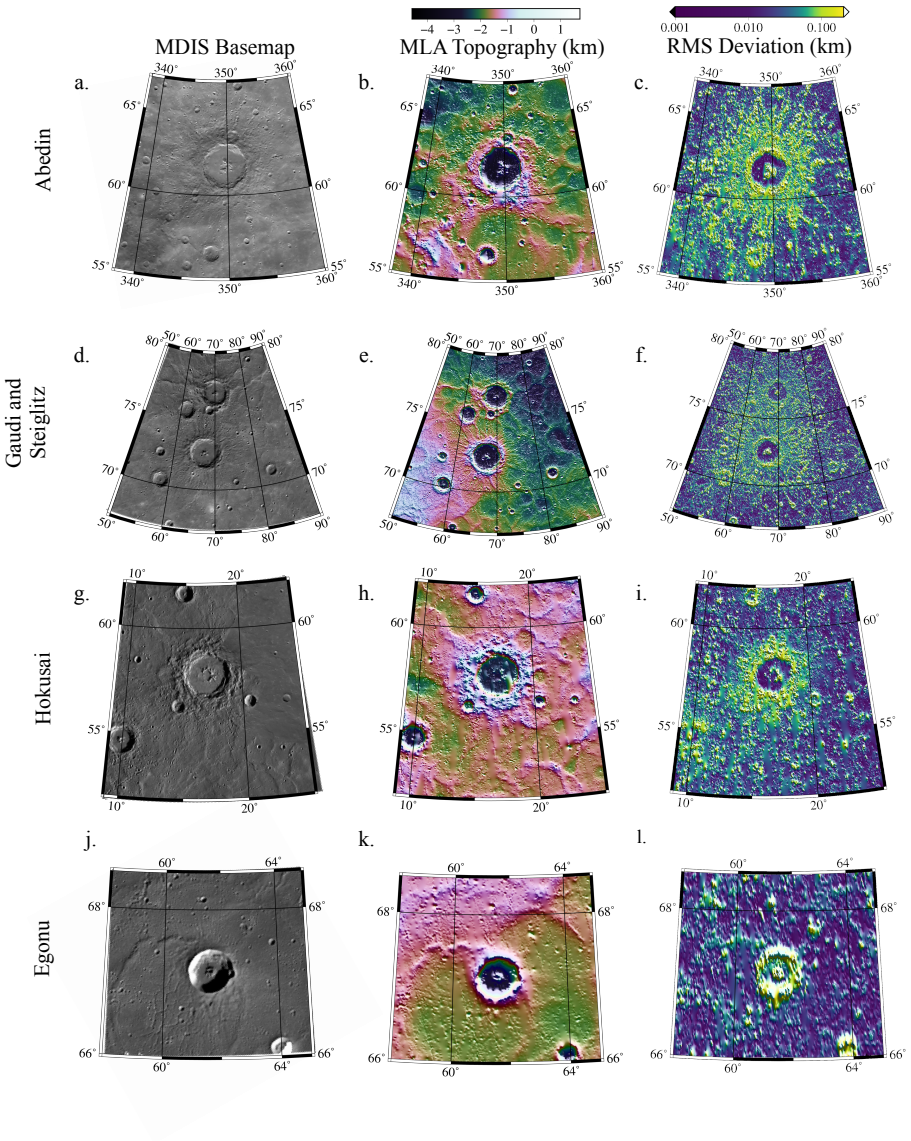

Figure 2. MDIS (Mercury Dual Imaging System) images (250 m/pixel basemap), MLA topography, and the $L = 1$ km surface roughness for 5 impact craters on Mercury. (d)-(f) combine the images for Stieglitz and Gaudi. The craters Abedin ($d = 122$ km), Gaudi ($d = 81$ km), and Stieglitz ($d = 100$ km) all show aerially broad regions of increased surface roughness beyond their rims. Hokusai ($d = 97.3$ km), similar in size to Abedin, does not have as large of a region of high surface roughness as Abedin. The crater Egonu ($d = 25$ km) does not show the same increased region of surface roughness surrounding the crater despite ejecta and secondary craters being visible in the MDIS image. Smaller craters might not produce sufficient fresh ejecta volume (or fragment size), nor fast enough secondary cratering to alter surface roughness significantly at the baselines investigated. Figure (l) appear more 'blurry' than (c) and (f) to

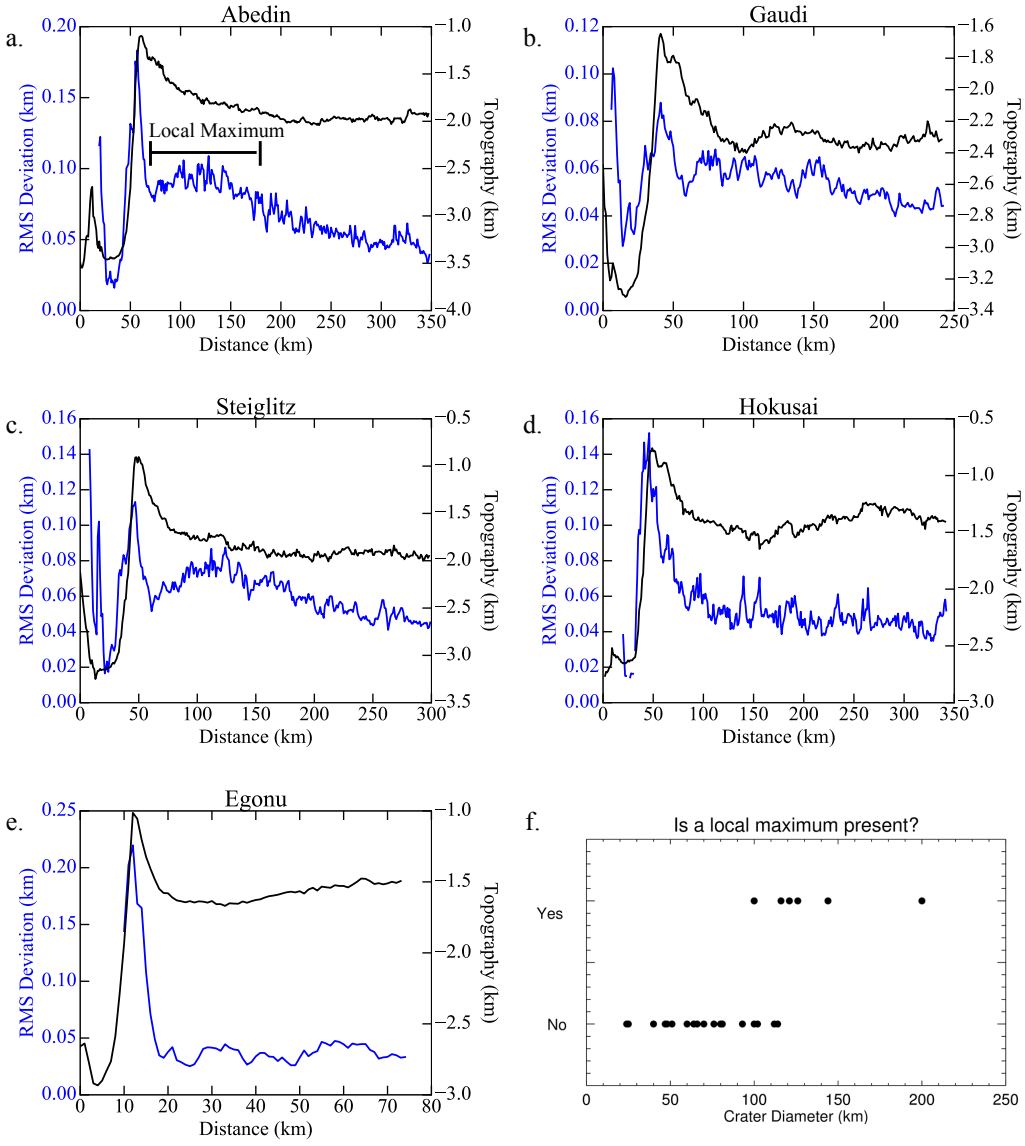

Figure 3. (a)-(e) RMS deviation for $L = 1$ km (blue) and MLA topography (black) as a function of radial distance from the crater center for large craters mapped in Figure 1. Note the qualitative local maximum present around Abedin and Stieglitz, the diameters of craters with and without the qualitative local maximum is plotted in (f). The Trask freshness criteria classification [1-5 with 5 the freshest *Trask and Guest*, 1975] for the craters above are Abedin = 4, Gaudi = 3, Stieglitz = 4, Hokusai = 5, and Egonu = 4.

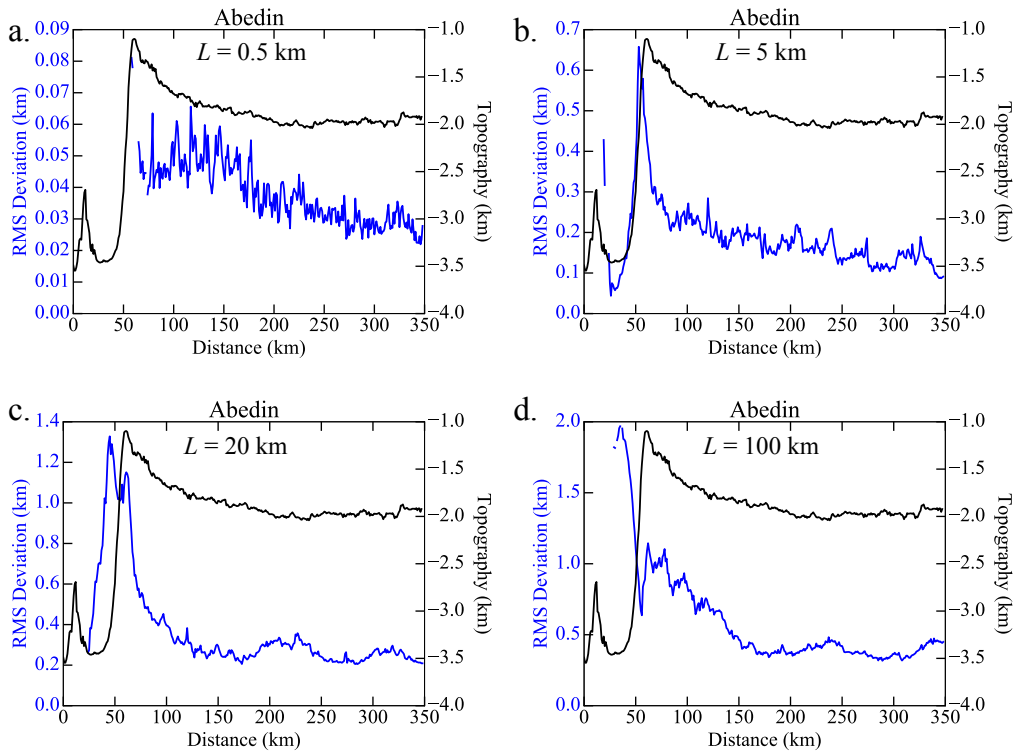

Figure 4. (a)-(d) RMS deviation and MLA topography in radial bins from the center of the crater Abedin for L = 0.5, 5, 20, 100 km. The qualitative local maximum is only present at L = 0.5 km and 1 km (previous figure). At L = 100 km there is only one peak in surface roughness for the crater due to the crater cavity itself.

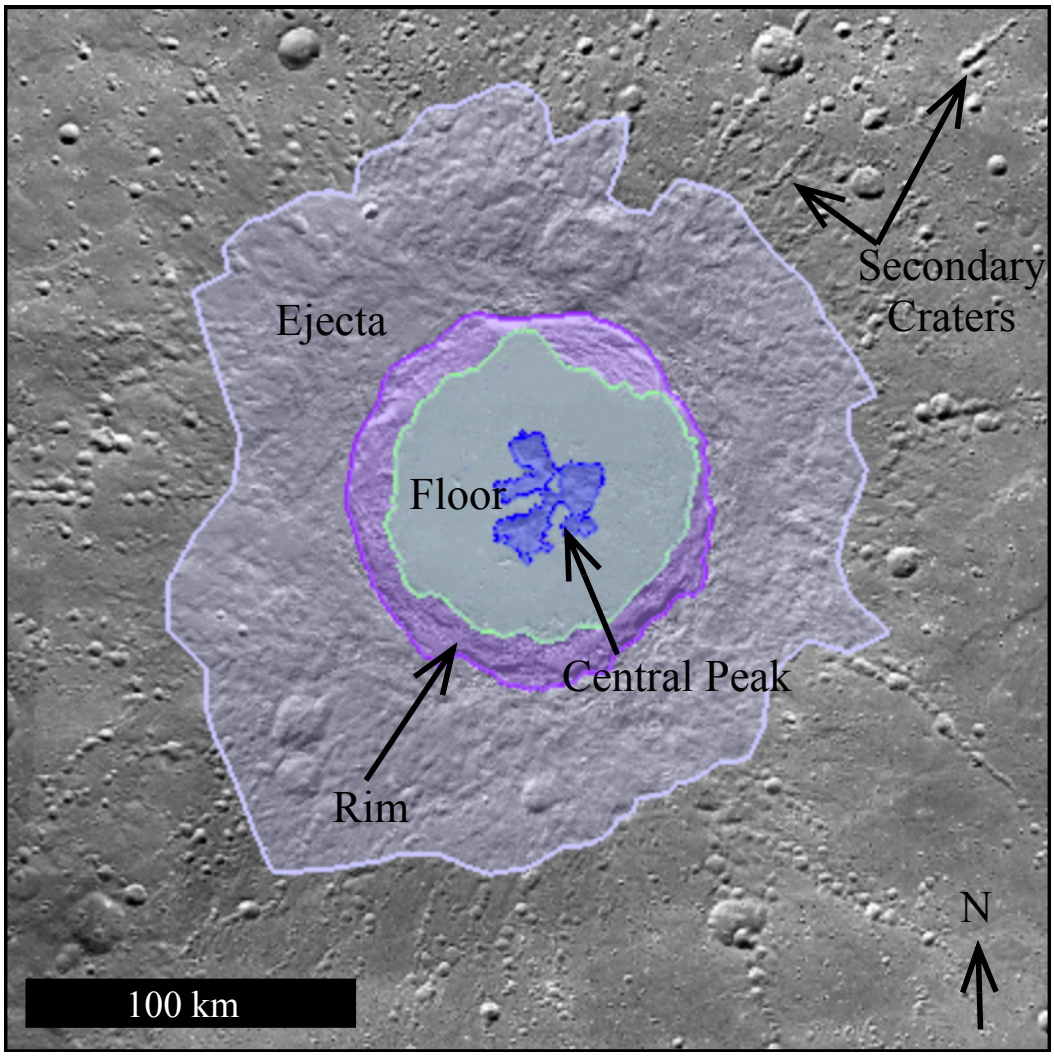

Figure 5. A geologic map of the crater Abedin. The ejecta, rim, central peak and crater floor are labeled. A few secondary craters are also identified. This map was used to guide identification of the source of the qualitative local maximum in Fig. 6.

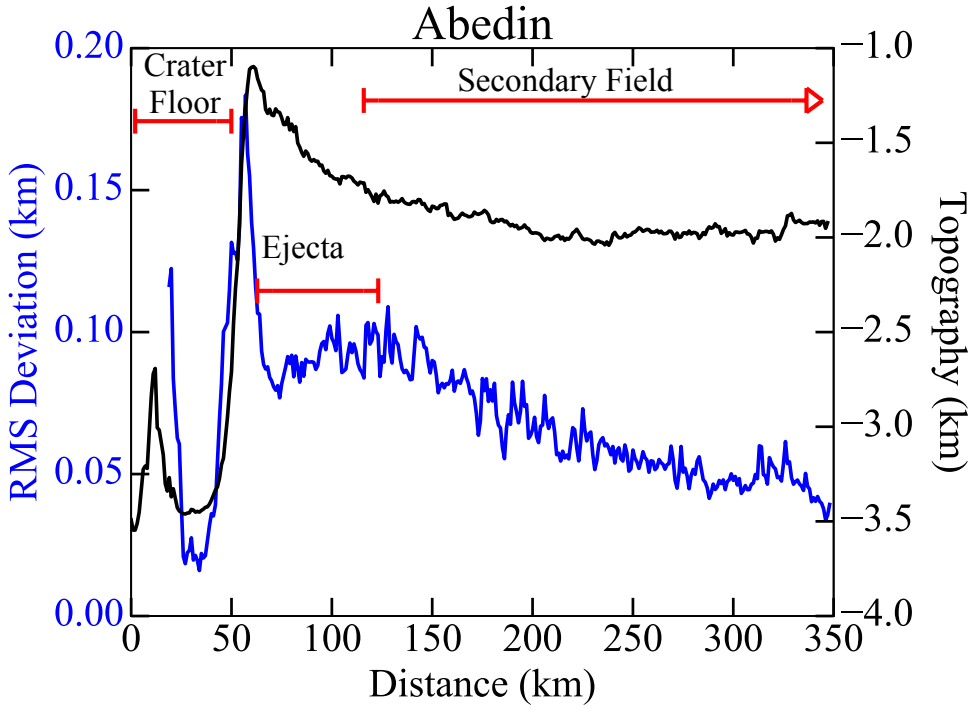

Figure 6. The RMS deviation at L = 1 km and MLA topography plotted radially from the center of the crater Abedin (same as Fig. 2(a)) with the radial range of the crater cavity, ejecta, and secondary fields identified.

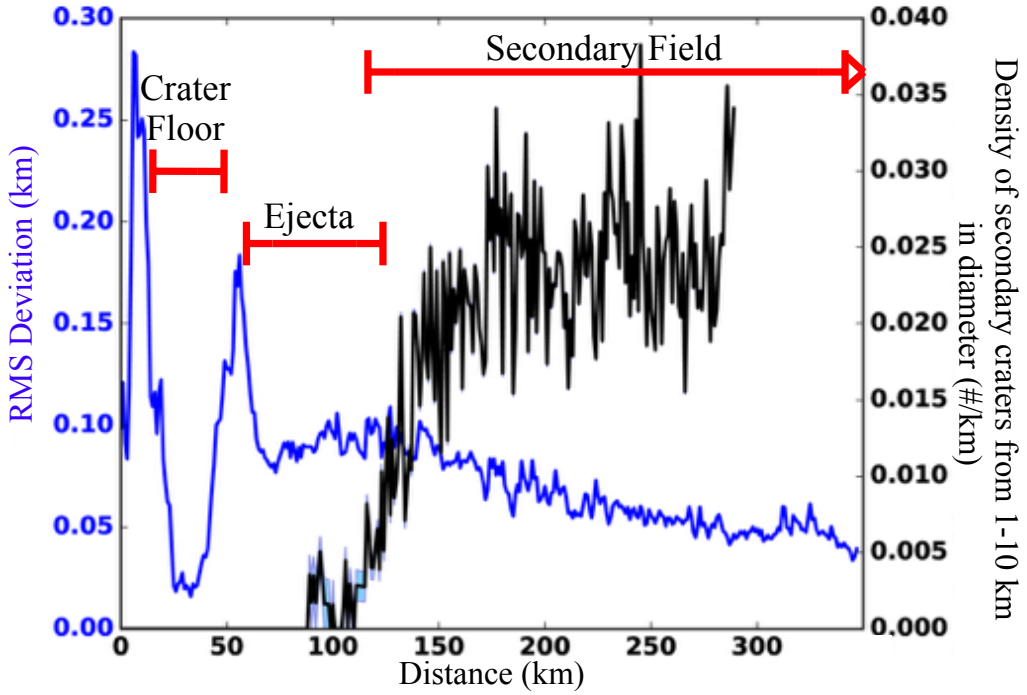

Figure 7. Radial surface roughness distribution for Abedin and the radial density distribution of secondary craters ranging in diameter from 1-10 km. The secondary crater density is truncated at a distance of 290 km away from the crater center since we were investigating the qualitative local maximum, which is closer to the crater center. The blue region represents a 1 sigma error bar. The radial mapped distance of the crater floor, ejecta, and secondary fields from Fig. 5 are added for reference.

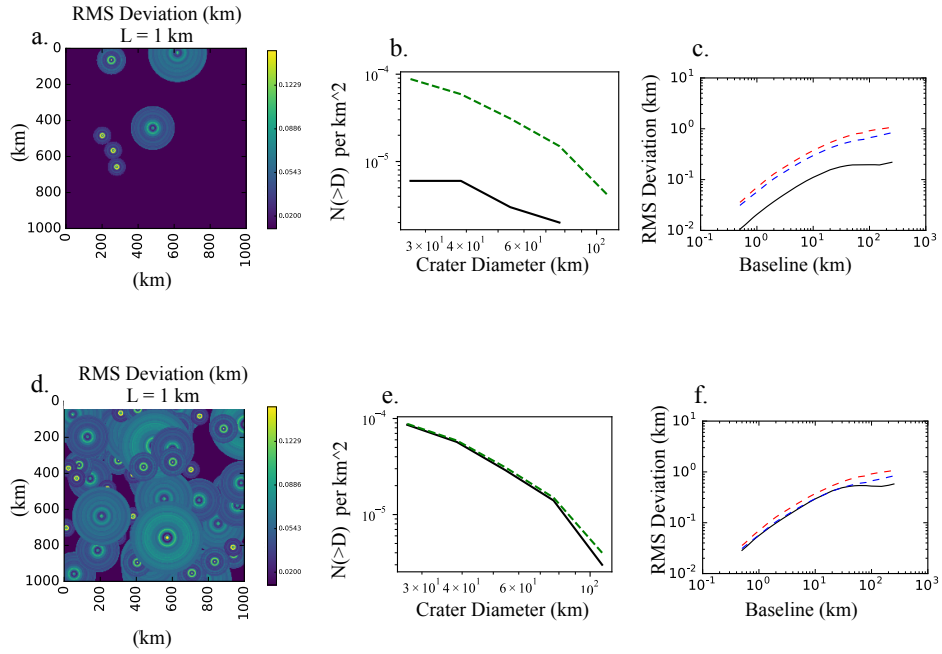

Figure 8. (a)-(c) Computed surface roughness obtained after 6 impact craters with diameters ranging from 25 to 120 km are emplaced on a 1000-km-by-1000-km surface where the initial surface roughness is set to zero. (d)-(f) is the same surface with 88 craters emplaced, this matches the size frequency distribution of impact craters with diameters between 25 and 120 km in a 1000-km-by-1000-km area for the cratered terrain [*Ostrach et al.*, 2015]. Maps of the surface roughness are shown in (a) and (d), while (b) and (e) show the number of craters per unit area at this point in the simulation (the black line is the target size-frequency distribution). Deviograms (c) and (f) show the calculated surface roughness of the entire 1000-km-by-1000-km region and can be compared to the observed surface roughness of the cratered terrain (red dashed) and smooth plains (blue dash) *Susorney et al.* [2017].

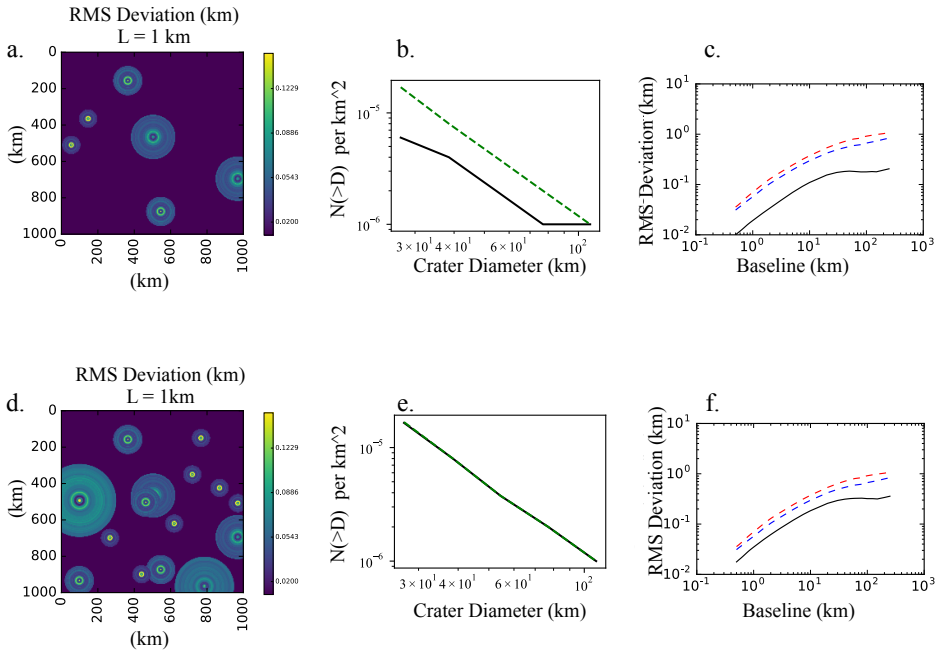

Figure 9. (a)-(c) Computed surface roughness obtained after 6 impact craters with crater diameters ranging from 25 to 120 km are emplaced on a 1000-km-by-1000-km surface where the initial surface roughness is set to zero. (d)-(f) is the same surface with 16 craters emplaced, this matches the size frequency distribution of impact craters with diameters between 25 and 120 km in a 1000-km-by-1000-km area for the smooth plains [*Ostrach et al.*, 2015]. Maps of the surface roughness are shown in (a) and (d), while (b) and (e) show the number of craters per unit area at this point in the simulation (the black line is the target size-frequency distribution). Deviograms (c) and (f) show the calculated surface roughness of the entire 1000-km-by-1000-km region and can be compared to the observed surface roughness of the cratered terrain (red dashed) and smooth plains (blue dash) *Susorney et al.* [2017].

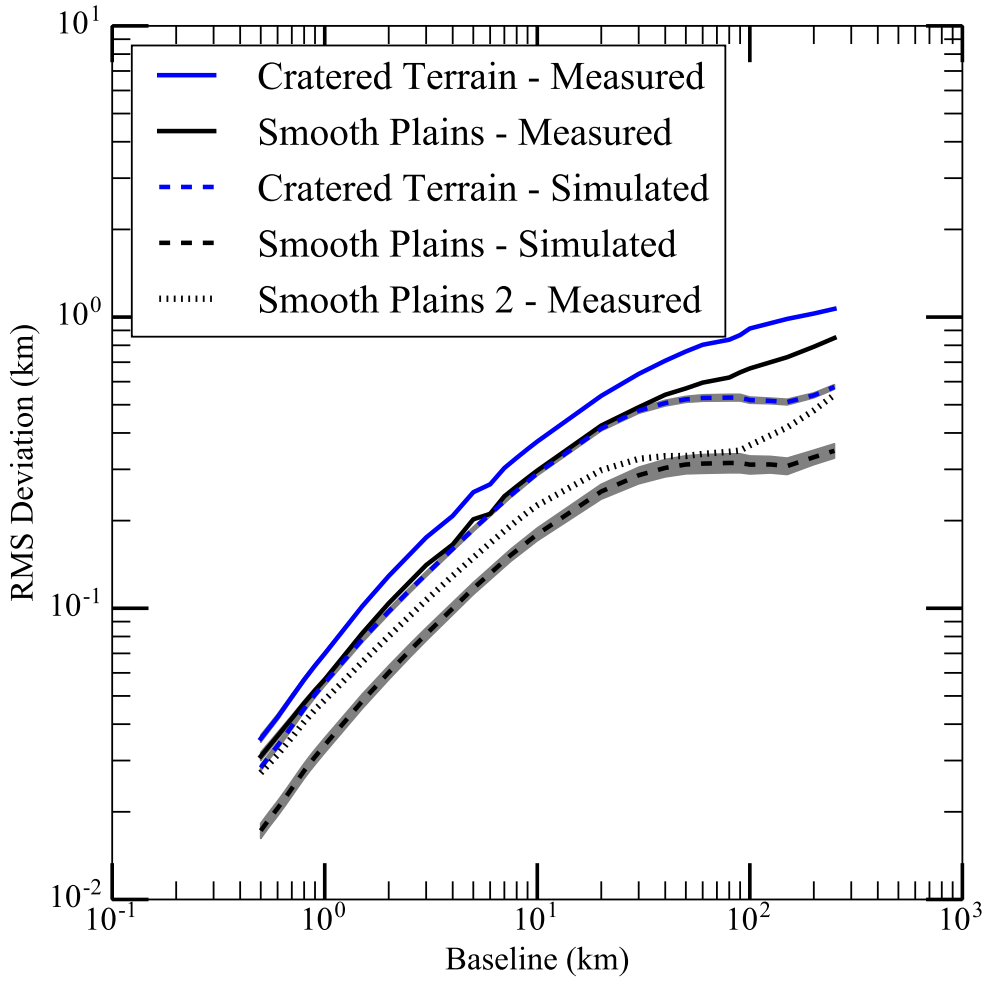

Figure 10. A deviogram of the measured [*Susorney et al.*, 2017] and simulated surface roughness for both the smooth plains and cratered terrains on Mercury. Uncertainties associated with the measured surface roughness are from the error of MLA measurements (<1 m) and are smaller than the thickness of the lines plotted. The mean simulated surface roughness of smooth plains and cratered terrains from 30 runs is plotted with a solid line. The gray shaded region represents the one standard deviation of the range of results obtained after 30 runs.

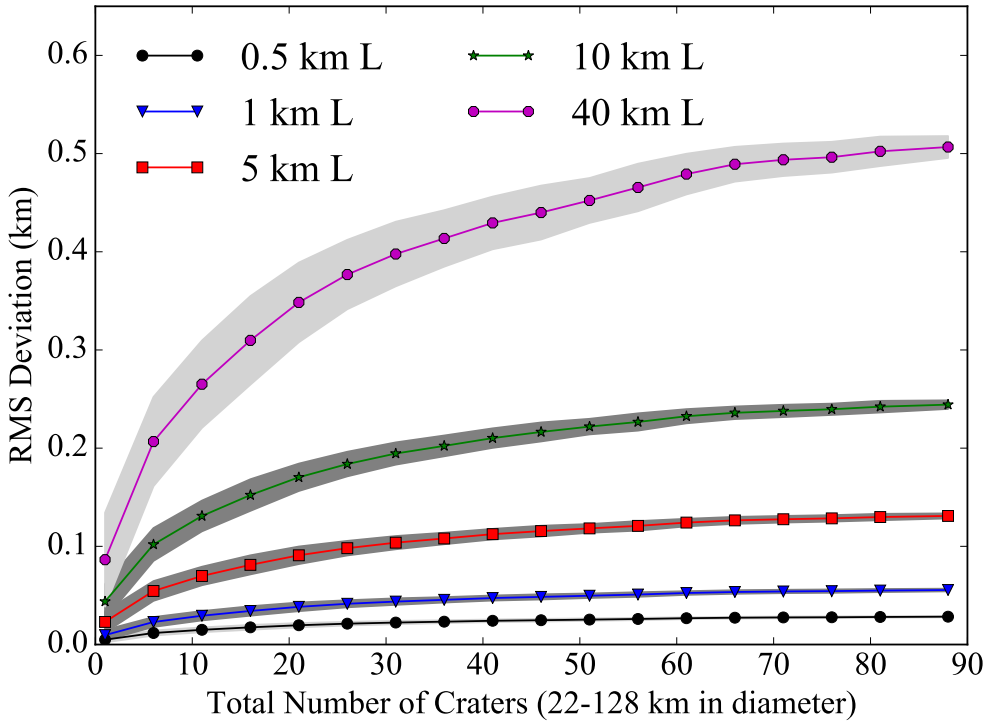

Figure 11. RMS deviation (or surface roughness) measured at five baselines (L) computed from the numerical investigation as a function of the total number of craters used in the computation (each point represents five additional craters emplaced in the investigation). The gray region is the one standard deviation for 30 runs employed. These simulations were run until surface roughness steady-state was reached.

Table 1. Characteristics of the five craters used in the numerical investigation. The freshness classification is scaled 1 - 5, with 5 being the freshest [e.g., *Trask and Guest*, 1975]. The frequency columns are the values from [*Ostrach et al.*, 2015] for the size bin each crater is represented in our model and SP refers to the smooth plains and CT refers to the Cratered Terrain.

Crater Name	Diameter (km)	Longitude (°W)	Latitude (°N)	Freshness Classification	Frequency for SP	Frequency for CT
Egonu	25.0	298.5	67.1	4	1.70×10^{-5}	9.16×10^{-5}
Rivera	40.0	327.8	69.3	4	8.23×10^{-6}	6.27×10^{-5}
Tung Yuan	60.5	62.8	75.0	3	3.94×10^{-6}	3.49×10^{-5}
Gaudi	81.0	290.8	76.9	3	2.15×10^{-6}	1.88×10^{-5}
Stieglitz	100	292.4	72.5	4	1.07×10^{-6}	7.36×10^{-6}